THE EFFECT OF BANDGAP ON LANTHANIDE SENSITIZATION IN II-VI SEMICONDUCTOR NANOPARTICLES

by

Robin F. Sloan

BS in Chemistry, Clemson University, 2006

Submitted to the Graduate Faculty of the

Dietrich School of Arts and Sciences in partial fulfillment

of the requirements for the degree of

Master of Science

University of Pittsburgh

2013

UNIVERSITY OF PITTSBURGH

DIETRICH SCHOOL OF ARTS AND SCIENCES

This thesis was presented

by

Robin F. Sloan

It was defended on

December 8, 2011

and approved by

Dr. Sunil Saxena, Associate Professor, Department of Chemistry

Dr. Haitao Liu, Assistant Professor, Department of Chemistry

Thesis Advisor: Dr. David H. Waldeck, Professor and Department Chair, Department of Chemistry

Copyright © by Robin F. Sloan

2013

THE EFFECT OF BANDGAP ON LANTHANIDE SENSITIZATION IN II-VI SEMICONDUCTOR NANOPARTICLES

Robin F. Sloan, M.S.

University of Pittsburgh, 2013

As nanotechnology continues to find its way into medical treatments, it is important to understand how to develop a bright imaging agent that will be more robust than current organic fluorophores. Key characteristics of inorganic lanthanide based materials, which are superior to current organic reporters, are their resistance to photobleaching, narrow emission bands, and long luminescent lifetimes; however their small radiative rate requires that they be sensitized. There are also multiple lanthanides that emit in the visible and near infrared region, allowing multiplex assays to be developed. Based on a model proposed by Mukherjee, et al.,[i] lanthanide emission is expected to show a dependence on the bandgap of the host nanoparticle material. The goal of this study was to examine this prediction. This study uses absorbance to determine the size and band gap of the host nanoparticles and uses XPS, EDS, and ICP to determine the dopant concentration. Using these measurements, the integrated time-gated luminescence is compared to the dopant percentage and bandgap of the nanoparticles. In agreement with the model, large bandgap materials are able to sensitize the terbium more efficiently, yielding brighter luminescence which is ideal for an imaging agent.

TABLE OF CONTENTS

LIST OF TABLES

LIST OF FIGURES

PREFACE

I would like to thank a number of people who have supported me throughout my time in graduate school. First, I must thank my advisor Dr. David Waldeck and my committee members Dr. Sunil Saxena and Dr. Haitao Liu. A big part of being able to perform research was to ask help of certain members of my research group: Dr. Prasun Mukherjee, Dr. Mingyan Wu, Dr. Kathryn Davis, Dr. Matthew Kofke, Daniel Lamont, Yang Wang, Xing Yin, Brian Bloom, Hao Lu, Madu Mendis, Brittney Graff, and my undergraduate researcher assistant Christopher Zimmerman. In addition to my research group, there were collaborators who worked on this project with me, and they include Dr. Stephane Petoud and Dr. Chad M. Shade.

I would also like to thank the professors who taught each of the courses I took: Dr. Adrian Michael, Dr. Nathaniel Rosi, Dr. Rena Robinson and Dr. Seth Horne.

For help with TEM, XPS, and other characterization techniques that aren't included in this thesis, I would like to thank Dr. Susheng Tan, Dr. Joel Gillespe, Tom Harper, Cole van Ormer, and Al Stewart for their assistance in training and running samples for me.

I must also thank staff members of the chemistry department who have helped me from the electronics shop, machine shop, and IT support: Tom Gasmire, Jeff Sicher, Chuck Fleishaker, and Jeffrey Flack.

Finally I would like to thank the staff members of the stockroom and main office for everything they do as well: Albert-John Krall, Devin Wilcox, Bill Grissom, Josh Jones, Michele Monaco, Mary Beth Conroy, Michael Pater, Mary Schwarman, Darlene Lanz, LaShawn Youngblood, Dawna Kasper, and Toni Weber.

1.0 INTRODUCTION

A need exists for a new generation of biological reporters that have better signal-to-noise ratio and characteristic deeper imaging capabilities in tissue than those currently available from organic dyes. Modern organic fluorophores are optically bright and inexpensive; however, they are susceptible to photobleaching making experiment repetition, or long experiment times, impossible.[ii] Photobleaching occurs when organic fluorophores are irradiated with light and oxygen radicals are created which can destroy the fluorophores and limit the amount of time for experiments. Without photobleaching, experiment times can be longer and tests can be performed repeatedly without deterioration of the luminescent sensor. The broad emission bands of organic dyes limit the discrimination between reporters in a single system. If emission peaks were sharper and spectroscopically discrete, multiplex assays could be developed using multiple reporters in the same optical window spanned by only one or two organic reporters. Organic fluorophores have nanosecond-lived fluorescence lifetimes whose emission is contaminated by short-lived native background autofluorescence.[iii]

Many of the current problems with organic biological reporters can be solved with lanthanide based nanoparticles. Inorganic materials are more resistant to photobleaching and thus allow for longer experiment times and repetition of tests without deterioration of the luminescent sensor.[1] A host semiconductor material, such as ZnS, does not decompose until temperatures of 400°C in air or oxidizing environments, so using these particles in a biological

system, with a temperature of 37°C, should be stable enough for repetitive testing. Organic complexes have incorporated lanthanides and display relatively high quantum yields, but only one lanthanide ion per organic molecule limits the amount of light per unit volume. In contrast, a nanocrystal host can incorporate many lanthanide ions, thus increasing the overall number of emitted photons per unit volume from these reporters. The brightness of quantum dots can also be 10-20 times higher than organic dyes, which gives a superior signal-to-noise ratio. Unlike organic fluorophores, which often have a small Stokes shift, lanthanides do not suffer from reabsorption of their emission. In the systems studied, lanthanides are excited with 300 nm light and terbium, which emits at the lowest wavelength, does not emit until ~490 nm, removing the possibility of reabsorption by the nanoparticle.

Additionally, lanthanides have luminescent lifetimes on the order of hundreds of microseconds to milliseconds, allowing time-gated luminescent spectroscopy to be used in order to isolate the luminescent signals from background emission, thereby increasing the sensitivity of detection. Figure 1 shows the excitation and emission spectra of CdSe:Tb nanoparticles. The steady state emission is broad, with no terbium emission observable; however, when time-gated spectroscopy is used, long-lived terbium emission is isolated (see blue line spectrum in figure 1). Two things can be noted from the excitation scans; there is significant overlap between the excitation scans and there is a lack of direct excitation bands. Both of these pieces of data suggest that CdSe is acting as an antenna.

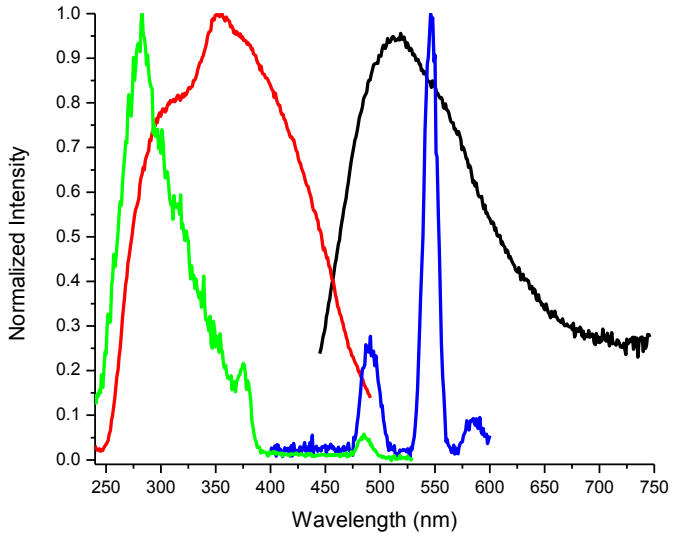

Figure 1: Normalized time-gated and steady-state excitation and emission are shown for CdSe:Tb The black and blue curves show the steady state and time-gated emission, respectively, when excited at 300 nm. The red and green curves show the steady state and time-gated excitation, respectively, while monitoring the 545 nm emission band.

To overcome their weak oscillator strength, lanthanides can be incorporated into a nanoparticle host. The host nanoparticle can function as an antenna with high oscillator strength, increasing photon absorption. This energy can be transferred to lanthanide ions, thereby sensitizing their emission. Because this process is more efficient than direct excitation of the lanthanide ions, the luminescence is stronger with an antenna present and the excitation profile of the luminescence matches that of the antenna chromophore. Although some free lanthanides can be somewhat toxic, encapsulating lanthanide ions into a host can eliminate this problem. The Ln^{3+} ions will remain bound at the surface, or within the core of the particles, mitigating their biological impact.

Lanthanides have many unique and advantageous properties that make them strong candidates for biological imaging and multiplexing or barcoding applications. The different lanthanides emit discretely over a large spectral range, spanning the visible and near infrared (NIR). Figure 2 shows the emission bands of several lanthanides, ranging from 400 nm (25000 cm^{-1}) to 1600 nm (6250 cm^{-1}). Figure 2 serves to show how, within a given range of the spectrum, several lanthanides can be incorporated into the same system, and allow for a unique spectral signature for use in multiplexing applications. Not only can multiple lanthanides be used, but also adjusting the relative amounts of each lanthanide in a system could enable a spectroscopic signature to be created. In this case, the relative intensities of emission bands would reflect the amount of each lanthanide added during synthesis. Such a barcode has been demonstrated in metal organic frameworks by incorporating three NIR emitting lanthanide ions, however, to my knowledge; a multi-lanthanide nanoparticle has not been developed through direct synthesis.

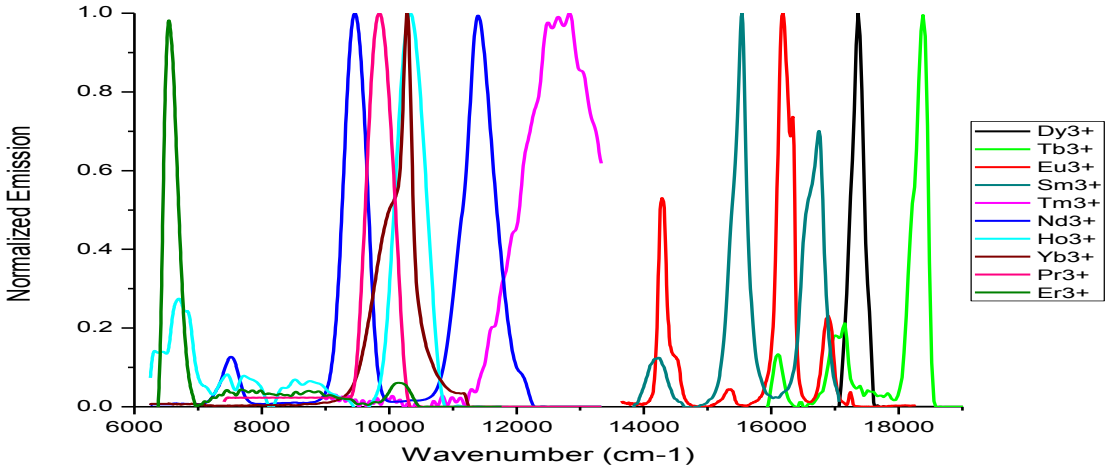

Figure 2: Emission spectra are shown for trivalent lanthanide ions, revealing sharp bands that span the visible and near infrared regions.

Trivalent lanthanides have characteristic emission spectra displaying sharps bands with energies that are weakly sensitive to changes in the environment, such as temperature, pH, and solvent. The observed transitions are rearrangements of the non-bonding 4f electrons, which are shielded by 5s and 5p shells. These 4f orbitals penetrate somewhat toward the core, but have minimal orbital exposure to the environment, preventing significant overlap with ligand and solvent orbitals. The cartoon in Figure 3 shows the relative location of the subshells within the lanthanide atom.

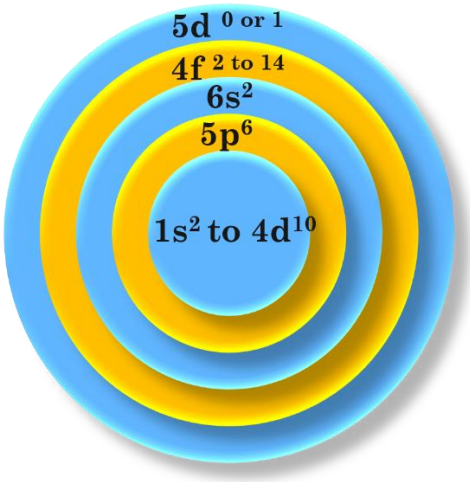

Figure 3: Electron shell configuration for Ln's showing the location of the 4f electrons.

As shown in Figure 4, biological species such as hemoglobin absorb strongly in the visible region and the optimal window for reporters in such biological media lies between ~650 nm and 900 nm.[iv] As wavelengths exceed 900 nm, the water present will begin to absorb more strongly and mask the signal. NIR light scatters less in biological tissues than visible light, allowing NIR light to penetrate tissue more deeply. According to a study by Park et al., images of lymph nodes in a pig were able to be seen at depths of 1 cm by using quantum dots emitting at 840 nm - 850 nm.[v] Generally, penetration depths are only a few millimeters for wavelengths below ~700 nm and because of the low absorption coefficient between 700 nm and 900 nm, light

can penetrate several centimeters in this region. The figure below suggests that in the NIR window with absorption coefficients ~0.1 cm^{-1}, depths of 10 cm should be obtainable, while visible wavelengths have absorption coefficients exceeding 1.0 cm^{-1}, and the penetration depth will be less than 1.0 cm. This shows how imperative it is to extend into the NIR for non-invasive imaging applications.

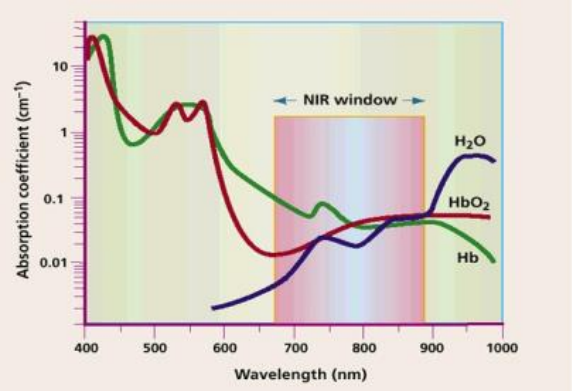

Figure 4: Absorption spectra of hemoglobin and water.[4]

By studying the properties of lanthanides and their hosts, we aim to develop imaging agents that overcome many of the limitations faced by current organic reporters. With photobleaching eliminated, longer exposure to irradiation can be achieved, allowing for better signal-to-noise and for multiple tests to be performed with the same reporters. Additionally, by incorporating many lanthanide ions into each nanoparticle host, we can increase the signal level and achieve superior brightness. This increased signal will allow for easier and more accurate detection of target systems. By taking advantage of the spectral range and long luminescent lifetimes, background contamination from intrinsic sample fluorescence can be eliminated from the emission signal, giving rise to greater sensitivity. Unambiguous recognition of these reporters is also possible because of their lack of sensitivity to environment, allowing for easy identification. Interference from visible absorbing molecules like hemoglobin can be reduced by extending into the NIR domain, allowing imaging applications in tissue.

1.1 GENERAL CHARACTERISTICS OF NANOPARTICLES

The band gap of a semiconductor is defined as the energy range that is not accessible to electrons in the material,[vi] due to quantization of energy. When light of sufficient energy is absorbed by a semiconductor it creates an electron-hole pair where the electron is excited to energy states above the bandgap and into the conduction band, leaving a hole in the valence band. Once an electron is excited into the conduction band, it may become unbound and free to move about the atomic lattice of the material, acting as a charge carrier. If its energy is low enough, it can be trapped by the Coulomb field of the valence band hole, forming a quasiparticle called an exciton. If the semiconductors exciton radius, the characteristic distance between an electron and its corresponding hole, is larger than the size of the nanoparticle, then quantum confinement effects are observed. The exciton radius can be calculated according to the following equation.

$$a_B = \frac{\epsilon_0 \epsilon h^2}{\pi \mu e^2} \quad (1)$$

where ϵ_o is the vacuum permittivity, ϵ is the dielectric of the material, h is Planck's constant, μ is the reduced mass, and e is the charge of an electron. The reduced mass is defined as:

$$\mu = \frac{m_e m_h}{m_e + m_h} \quad (2)$$

where m_e and m_h are the effective masses of the electron and hole, respectively.[vii] For CdSe nanoparticles, using m_e=.13m_o and m_h=.44m_o and a dielectric constant of 9.3,[viii] the exciton radius is ~4.9 nm, meaning that any particle with a diameter smaller than ~10 nm will express quantum confinement. Particles must be on the nanometer scale for confinement to be observed, and based on growth dependence studies, these particles can grow quickly. After nucleation, approximately two minutes elapse before the particle growth terminates, as is seen in the fluorescence and absorption measurements.

Because of the low number of atoms in each nanoparticle, they may contain discrete energy states much like molecules, as demonstrated in Figure 5. As the number of atoms in a nanoparticle increases, more energy levels begin to overlap and form a band, as in bulk materials. Using the particle in a box analogy, an electron-hole pair behaves as if it were trapped in a box with a potential barrier at the walls, confining the exciton to the inside of the box. Because the length of the box is smaller than the exciton radius, the nanoparticle's exciton has a smaller spatial extent and hence a higher kinetic energy than its unconfined counterpart, which causes an increase in the optical bandgap of the semiconductor nanoparticle, as compared to the bulk material. Because these energy levels are quantized, spectroscopy can now reveal defined energy states in absorption and emission spectra, instead of one broad peak. This confinement

effect also leads to a hypsochromic shift in both the absorption edge and the photoluminescence signal at shorter growth times.[ix,x] This shift in the bandgap can be estimated by the effective mass approximation:

$$E_g(nano) \approx E_g(bulk) + \frac{\hbar^2\pi^2}{2R^2}\left[\frac{1}{m_e} + \frac{1}{m_h}\right] - \frac{1.8e^2}{\varepsilon R} \quad (3)$$

E_g is the bandgap energy, $\hbar$ is the reduced Planck's constant, R is the radius of the particle, m_e and m_h are the effective mass of the electron and hole, respectively, e is the charge of an electron, and ε is the dielectric constant of the material. [xi] The bulk bandgap is altered by two terms: the first being the excess kinetic energy, and the second being the electrostatic attraction between the electron and hole pair.

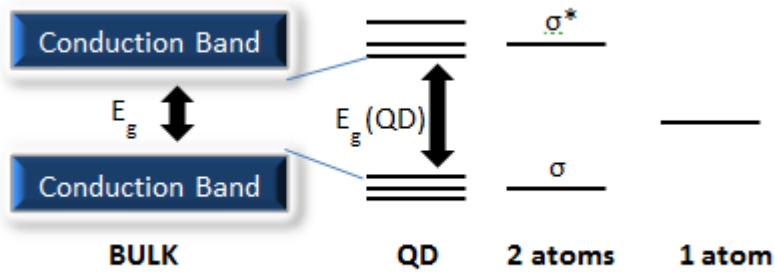

Figure 5: This cartoon shows the emergence of discrete energy levels when going from bulk to the quantum confinement regime, and finally to atoms. Another important feature is the increase in band gap in the QD regime

As the nanoparticles grow, the exciton becomes less confined and the photoluminescence peak wavelength begins to red-shift until the bulk material value is reached as illustrated by the cartoon in Figure 6.

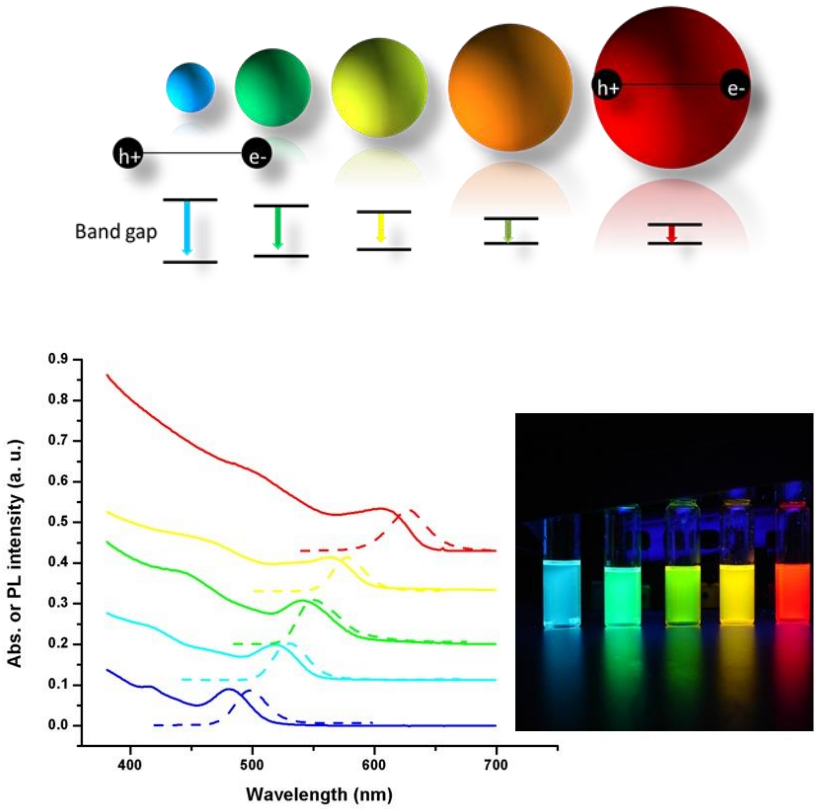

Figure 6: (Top) This cartoon illustrates the quantum confinement effect. As particles grow their bandgap emission red-shifts until the bulk energy is reached. The bulk limit is reached when the size of the particle is the size of the exciton. (Bottom) Example of quantum confinement effects in CdSe particles. Solid lines are absorption spectra and the dotted lines are photoluminescence spectra.

If a hypsochromic shift of the absorption and photoluminescence spectra is observed from the bulk material, we can interpret this is to signify the presence of nanoparticles expressing quantum confinement. Figure 6 illustrates the quantum confinement effect for CdSe nanoparticles. The bulk bandgap is 1.7eV, which corresponds to an absorbance peak at 730 nm. The spectra in figure 6 clearly show a hypsochromic shift of the bandgap with decreasing growth time, and decreasing size of the particle. Comparison of the spectral shifts of the first exciton band, λ_{max}, with the nanoparticle size, which are measured by transmission electron microscopy

(TEM), can be used to quantify the particle diameter, *D*. An empirical fit for CdSe data of this sort gives

$$D = 1.6122 \times 10^{-9} \lambda^4 - 2.6575 \times 10^{-6} \lambda^3 + 1.6242 \times 10^{-3} \lambda^2 - 0.4277 \lambda + 41.57 \quad (4)$$

where *D* is the diameter of the particle in nm, and λ in nm is the excitonic peak obtained from UV-Vis measurements.[xii] The exciton radius of CdSe nanoparticles is estimated to be 5.4 nm (m_e=.13m_o, m_h=.44m_o, and ϵ=10.2) and confinement effects should be seen in nanoparticles less than ~10 nm in diameter. Using equation 4, the particles in Figure 6 are calculated to range in size from 2.14 to 5.91 nm in diameter. Similar equations for CdS and CdTe were obtained based on fits relating the exciton peak location and sizes taken from TEM.[xiii]

1.2 LANTHANIDE CONTAINING NANOPARTICLES

Lanthanides are the elements ranging in atomic number from 58 to 71. The trivalent state is the common and stable ionic form for most lanthanides, and the 4*f* subshell is unfilled, but shielded from the environment by the 5*s* and 5*p* shells. Samarium, europium, thulium, and ytterbium are stable in divalent oxidation states, while cerium, praseodymium, and terbium are stable in a tetravalent state. Luminescence of the trivalent ions is of great interest because of their unique characteristics. Because the *f*-electrons are not involved in binding and are shielded by 5*s* and 5*p* shells, their emission spectra are sharp and do not shift their energies significantly with environment. The intensities may change, but the wavelengths typically show no

significant shifting. The trivalent lanthanides have Laporte forbidden transitions, which states *p-p*, *d-d*, and *f-f* transitions are forbidden. This forbidden nature gives rise to their low oscillator strength, long-lived luminescent lifetimes, and sharp emission bands.

The transition moment integral between the ground and excited states can be written as:

$$M = \int \psi_f'^{*}\, \hat{\mu}\, \psi_i \, d\tau = e \int_0^{\infty} r^2 dr \int_0^{\pi} \sin\theta d\theta \int_0^{2\pi} \varphi'^{*}_{n',l',m'} \vec{r}\, \varphi_{n,l,m} \, d\Phi \quad (5)$$

where $\hat{\mu}$ is the transition dipole moment operator and $\psi_f'^{*}$ and ψ_i are the wavefunctions of the excited and ground electronic states. *e* is the elementary charge, *r*, θ, and Φ are the radial and angular electron coordinates. If the value of M is zero, then the transition is forbidden. Because the electric dipole moment operator is odd, the integrand in Eqn. 5 is an odd function unless the angular parity of the wavefunction changes sign. Because $\Delta l = 0$ for *f-f* transitions, the transition is formally forbidden. In the presence of a ligand-field, an induced electric dipole transition becomes partially allowed due to the mixing of electronic states of opposite parity.[xiv]

Although lanthanides have many desirable properties, they also have several limitations. Organic fluorophores can have molar extinction coefficients of $>10^4$ $M^{-1}cm^{-1}$, while lanthanide ions are generally <10 $M^{-1}cm^{-1}$ because of the nature of the Laporte forbidden f-f transitions.[xv] This intrinsic characteristic makes it difficult to observe a strong emission signal through direct excitation. However, if we introduce lanthanide ions to a host material that can strongly absorb photons and transfer the energy non-radiatively to the lanthanides accepting energy levels, we can circumvent this limitation. This technique is called the antenna effect, and is illustrated by the cartoon in Figure 7. Evidence of the antenna effect taking place can be observed

spectroscopically. Referring back to Figure 1, the excitation spectra of the CdSe emission and Tb^{3+} emission are shown to overlap, suggesting that the excitation is the same for both the nanocrystal and lanthanide. The lack of structure in the nanocrystal excitation spectrum, i.e., a lack of discrete excitation bands of the terbium ion, shows that the nanocrystal acts as an antenna. Another example of the broad excitation profiles for CdSe:Tb nanoparticles is shown in figure 22 in the Appendix.

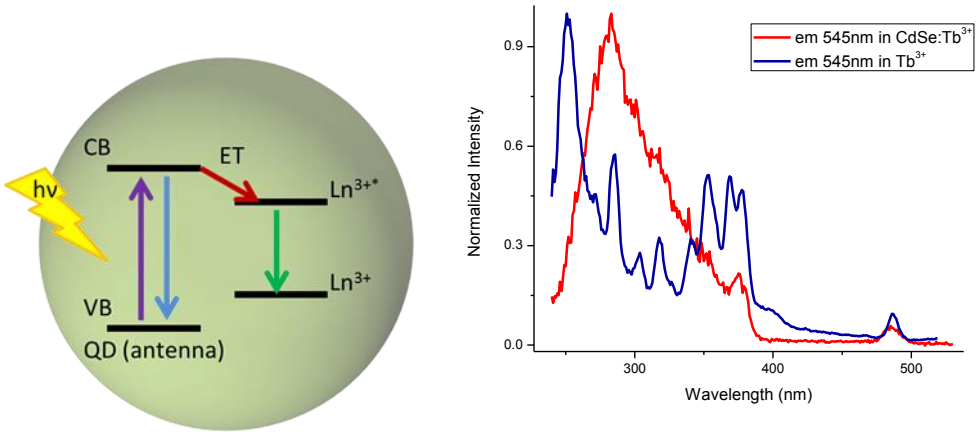

Figure 7: (Left): This cartoon shows energy transfer (ET) from the antenna to the Ln^{3+} center, upon absorption of light from the valence band (VB) to conduction band (CB). (Right): Resulting excitation spectra. The blue line shows many direct excitation bands of the 545 nm terbium emission when terbium is present as an ion in solution while the red band demonstrates the same emission band's excitation broadening due to the antenna effect.

Once the lanthanide excited state is populated, several deactivation pathways, both radiative and non-radiative are possible. The dominant non-radiative pathway for molecular complexes of lanthanides in solution is collisional energy transfer to solvent and the vibrational overtones of –CH, –NH, and –OH bonds.[xvi] The antenna not only has to absorb and transfer energy, but it must also act as a shield to limit the interactions of the lanthanides with ligands and solvent molecules which provide these non-radiative decay pathways. When a nanoparticle is used as a host, the vibrations of the lattice are very low frequency;[xvii] ~180 cm^{-1} for CdSe[xviii] in

comparison with ~3000 cm^{-1} to 3600 cm^{-1} for the solvents.[xix] As a result, the non-radiative decay rates of the lanthanides are significantly slowed, and we can observe a difference in core and surface lanthanide ions with the lanthanides in the core having a longer luminescent lifetime because of the elimination of high frequency non-radiative decay pathways.

Energy transfer from the nanoparticle excited state to the lanthanide excited state is not explained by Förster or Dexter type mechanisms. In a nanoparticle host, the mechanism by which energy is transferred to the lanthanides involves charge carriers. For the Tb^{3+} doped ZnS nanoparticle an electron is excited to the conduction band in the host leaving a hole in the valence band. Because the electron is now in a higher energy state, it can transfer to the unfilled orbital of the Tb^{3+}, while the hole is also attracted by the Tb^{3+} electron acceptor state, thus localizing the exciton on the trap state. This localization of the electron and hole on the terbium center can lead to the creation of the $^5D_4$ excited state in Tb^{3+} which decays radiatively back to the Tb^{3+} ground state. Figure 8 illustrates an energy level model for a mechanism proposed by Mukherjee *et al*., to explain the energy transfer from the II-VI semiconductor materials to the Tb^{3+} ions.[xx]

Dorenbos has been able to predict the energy levels of the lanthanides in different systems by compiling data from a large collection of compounds. Because there has been extensive research on the optical absorption and luminescence excitation spectra for europium, all initial calculations were performed for this lanthanide. The relative energies of the divalent and trivalent lanthanides are assumed to follow a well-defined trend which is largely based on the orbital filling pattern through the *f*-orbitals. These energy level trends in the lanthanide series allowed for relative energy levels of the other lanthanides, including terbium, to be determined. Thus by positioning the energy level of the Eu^{2+} to the valence band of the host semiconductor,

the other lanthanide ions energy can be known. For our purposes, two host-dependent parameters should be considered: the charge transfer energy from the host valence band to Eu^{2+} and the band gap of the host.[xxi] Because the anion of the host is largely responsible for the valence band position, the charge transfer energy from the anion valence band to Eu^{2+} should be determined.[xxii] For example, in sulfides, the energy difference between Eu^{2+} and the valence band is estimated to be 2.17 eV, so that the relative energy levels of all the lanthanides in the divalent and trivalent state can be set, within ~0.5 eV.[1] The energy difference in Eu^{2+} and Eu^{3+} is held constant at 5.7 eV for all systems we have studied.

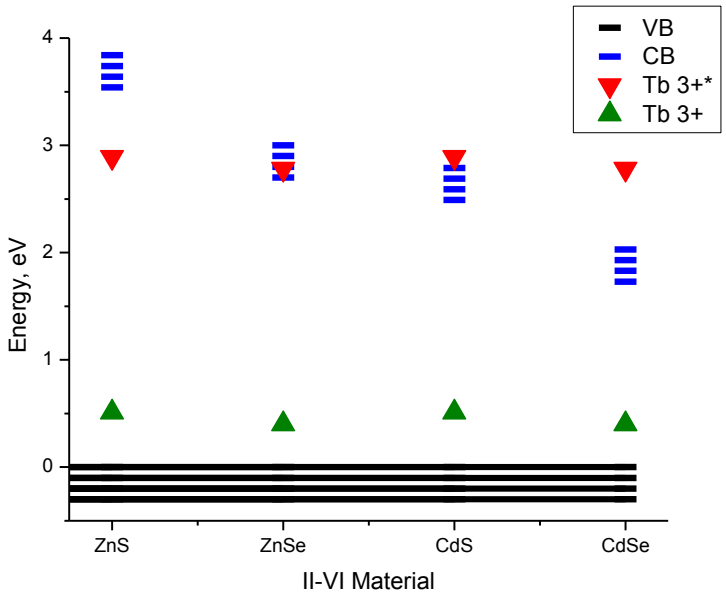

Figure 8: This diagram shows the predicted energy level alignment of Tb^{3+} in different host materials. Ground and excited states of $Tb^{3+}(f^8)$ are shown for different II-VI materials. The valence band of each material has been arbitrarily set to 0 eV

[1] There was a small distribution in charge transfer energies for each anion that can lead to error in energy level assignments. This distribution was largest in oxides.

Figure 8 shows the energy level scheme predicted for Tb^{3+} in four different bulk II-VI materials. From this model, we see that the ground and excited states of Tb^{3+} lie within the bandgap of ZnS. Terbium (III) can act as a hole trap in materials with their valence band below the ground state of the terbium, and this appears to be so for each of the materials. Because of quantum confinement effects the bandgap will be larger than what is shown in the diagram here. Thus, the sensitization efficiency of Tb^{3+} (f^8) should increase with decreasing nanoparticle size in hosts that have a bulk conduction band edge near or below the accepting level of the terbium. As the band gap increases, the energy level of the conduction band can surpass the energy of the lanthanide excited state and make the possibility of electron trapping more favorable; thus enhancing the energy transfer to the Tb^{3+} state. Because of a decrease in competing non-radiative pathways from autoionization, the luminescence yield from this excited state should increase. This effect should be observed in ZnSe, CdS, and CdSe systems where the bulk conduction band edge lies below the accepting level of the terbium ion.

By understanding nanocrystals' HOMO and LUMO energy levels with respect to the lanthanides, we can choose the appropriate host to sensitize different lanthanides. We should also be able to take advantage of the nanocrystals' tunable properties by controlling the size of the particles through synthesis. In doing so, we can control the band gap which is correlated to the sensitization efficiency and optimize the energy alignments in order to give the most intense luminescent signal from the lanthanide dopant. After gaining insight into the sensitization of the visible emitting lanthanides, we hope to apply this knowledge to NIR emitters.

2.0 EXPERIMENTAL PROCEDURES

2.1 SYNTHESIS

2.1.1 Materials

Trioctylphosphine (TOP, 90%), trioctylphosphine oxide (TOPO, 90%), cadmium oxide (CdO, 99.99%), hexadecylamine (HDA, 98%), oleylamine (OLA, 70%) were purchased from Sigma-Aldrich, St. Louis, MO. Spectroscopy grade chloroform was purchased from J.T. Baker, Phillipsburg, NJ. Sulfur, sodium hydroxide, methanol and toluene were purchased from Fisher Scientific, Pittsburgh, PA. Terbium (III) acetate hydrate (99.9%), and terbium (III) nitrate hydrate (99.9%) were purchased from Alfa Aesar, Ward Hill, MA. Selenium (Se, 99.99%), and tetradecylphosphonic acid (TDPA, 97%) were purchased from Strem Chemicals, Newburyport, MA. Argon was purchased from Matheson, West Mifflin, PA. All chemicals were used as received without further purification.

2.1.2 Experimental Setup

The reaction set up is as pictured in figure 9 below. A three-neck round bottom flask was used for nanoparticle synthesis. One neck held a reflux condenser and kept the reaction under argon. The other two necks were sealed off with septa. One septum held a thermocouple which

controlled the temperature of the reaction. The final neck/septum was used for injections of reaction precursors through a syringe. The entire vessel was situated in a heating mantle.

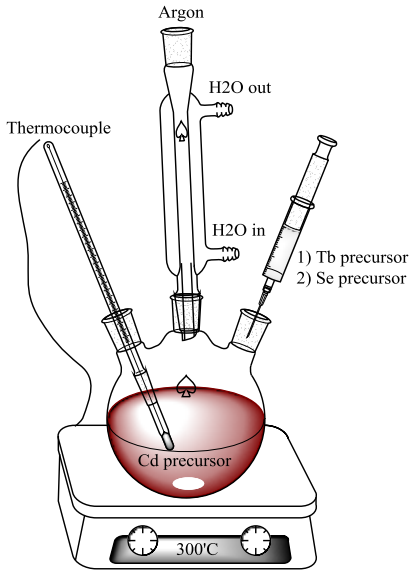

Figure 9: A cartoon of the reaction setup is shown. A heating mantle fitted with a thermocouple was used to control the temperature. The reaction vessel was kept under reflux and an Ar atmosphere.

2.1.3 Doped Nanoparticle Synthesis

Terbium-doped CdSe particles were synthesized by solvothermal methods. 10 mmol TOPO, 0.8 mmol TDDA, and 1.0 mmol CdO were loaded into a three-neck flask with a stir bar. The flask was fitted a with silicone septum on each of the side necks, and the center neck was fitted to a condenser. The condenser was connected to a Schlenk line for evacuating and purging the reaction vessel. A thermocouple was inserted into the reaction mixture to monitor the temperature and was interfaced with a temperature controller. Figure 9 shows a cartoon of this reaction set-up. The reaction mixture was heated to 100°C and degassed by vacuum pumping at 10 mTorr for several minutes. Next, the reaction mixture was purged with argon

and the temperature was increased to 300°C. Once the solution had become clear, which was usually overnight, a mixture of 0.6 mmol terbium nitrate and 4.0 mL TOP were injected at once. After one hour, the temperature controller was set to 230°C and the selenium precursor was injected (1.0 mmol Se powder and 4.0 mL TOP). Aliquots were removed immediately via a glass syringe.

2.1.4 Purification

Once aliquots were removed from the reaction vessel, 5 mL of butanol was added to maintain a solution (TOPO will resolidify). To this mixture ~10 mL of methanol was added and the sample was then centrifuged. The supernatant was discarded, and the precipitate was kept. To this precipitate, 1 mL of butanol was added again, vortexing if necessary to dissolve all the solid species. Again, methanol was added in excess (~10 mL) and the sample was centrifuged. The supernatant was discarded and the solid was dissolved in 2 mL of octanol, vortexing if necessary. This solution was then centrifuged and the supernatant was transferred to a new vial, and the precipitate was discarded. To this octanol mixture, 1 mL of ethyl acetate was added, and then ~15 mL of methanol. Finally, the sample was centrifuged again, and the supernatant was discarded. The precipitate was dried in a vacuum oven at 40C for 1 hour to remove any excess solvents. These dried nanoparticles could then be resuspended in the desired solvent for spectroscopic studies. In this case, spec grade chloroform was used.

2.2 INSTRUMENTATION

2.2.1 Absorption UV-Vis Spectrometer

An Agilent 8453 UV-Vis spectrometer was used for all absorption measurements. Absorbance spectra were collected over a wavelength range from 200 nm to 1100 nm. Initially a blank of the solvent was taken in the cuvette, followed by the nanoparticle containing sample. All samples were kept to similar absorbancies at their exciton peaks to ensure an approximately equal concentration of all samples tested. All emission spectra were corrected for varying optical density by dividing by the absorbance value at the excitation wavelength (300 nm).

2.2.2 Time-Gated Fluorimeter

A Varian Cary Eclipse was used for all time-gated luminescence measurements. The total decay time was set to 0.020 s, the delay time was set to 0.1000 ms, and the gate time was set to 5.000 ms. The excitation wavelength used was 300 nm, and the emission monochromator was scanned from 450 nm to 650 nm with a 1 nm data interval. The averaging time was 0.10000 s with a PMT voltage of 800 V. Entrance slits were 10 nm while exit slits were maintained at 5 nm.

2.2.3 Transmission Electron Microscope

The transmission electron microscope (TEM) used was located in the Nanoscale Fabrication and Characterization Facility (NFCF) at the University of Pittsburgh. It was a JEOL JEM-2100F capable of 2nm resolution. Sample preparation included placing a drop of the purified nanoparticle solution in a highly volatile solvent directly onto the copper TEM grid. The grid itself was on a kimwipe which allowed for excess solvent to be wicked away from the copper grid. Once the solvent had evaporated, the grid was placed in a plastic carrier for transport in order to avoid damaging or contaminating the sample.

2.2.4 Energy Dispersive X-Ray Spectrometer

The energy dispersive X-Ray spectrometer (EDS) was coupled to the TEM located in the NFCF. An accelerating voltage of 200kV was used for all measurements as well as a silicon detector. The acquisition geometry had an elevation of 25 degrees, while the tilt and azimuth were both 0 degrees.

2.2.5 Inductively Coupled Plasma Atomic Emission Spectrometer

A Perkin Elmer Optima 700DV inductively coupled plasma (ICP) with an atomic emission spectrometer (AES) with a charge coupled device (CCD) detector was used for all ICP measurements. The flow rate was set to 1.5 mL/min and samples were tested in triplicate. Yttrium was chosen as the internal standard and was used for all measurements. A deionized water blank was also used and subtracted from all emission intensities. Calibration curves were

made from cadmium, selenium, and terbium standards in 2% nitric acid. Primary emission wavelengths were used for all elemental composition analysis.

2.2.6 X-Ray Photoelectron Spectrometer

XPS spectra were collected on an in-house built instrument utilizing a Leybold EA10 hemispherical energy analyzer operating with a constant 50 eV pass energy. All experiments were performed at a base vacuum of $1x10^{-9}$ Torr or better and used the K-alpha line of Al for X-ray excitation (1487eV). Samples were cleaned prior to analysis with a 5 kV argon ion gun. Data was collected in 1 eV steps, with a step time of 1000 ms. Binding energies were scanned from 0 to 1000 eV. The work function of the spectrometer was 2.6 eV. Solid purified nanoparticle powder was placed on an epoxy resin fixed to tantalum foil. This foil was fixed to a copper plate that fit into the XPS and was able to be aligned with the X-Ray source.

3.0 LANTHANIDE CONTAINING NANOPARTICLES

3.1 RESULTS/DISCUSSION

3.1.1 UV-Vis Measurements

Once the nanoparticles were purified, spectroscopy studies were performed. Absorption measurements were taken to determine the size of the particle as well as the band gap. The absorption maximum peak position, not the onset, was used in determining the band gap for the associated nanoparticles. The shape of the spectra also allows one to see the relative size distribution and quality of the particles.

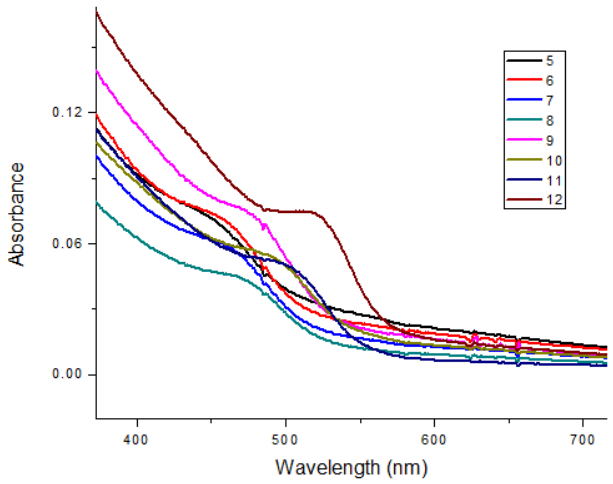

Sample	λ_{max} (nm)	λ_{max} (eV)	Diameter (nm)
5	453	2.72	1.97
6	459	2.69	2.02
7	461	2.68	2.03
8	471	2.62	2.10
9	478	2.58	2.16
10	491	2.51	2.26
11	501	2.46	2.35
12	517	2.39	2.53

Figure 10: (Left) Absorption spectra of aliquots pulled from the reaction after injection of Se precursor. 5-12 represent the order the aliquots were removed from the vessel and a general shifting trend in the exciton peak is observed. (Right) This table identifies the peak position of each aliquot and shows the corresponding bandgap and particle size.

The absorption spectra in figure 10 show a red-shift in the first exciton absorbance with the growth time and figure 21 in the Appendix shows a second example of this trend. As aliquots are removed from the reaction vessel, the particle growth is halted because the heat is removed. Peak positions for this particular reaction ranged from ~453 nm to ~517 nm, which corresponds to a diameter range of 1.97 to 2.53 nm, respectively. This range also shows us the change in bandgap from 2.72 to 2.39 eV, respectively. Thus, an analysis of the terbium ion intensity of each aliquot should reflect its dependence on the nanoparticle bandgap. As the results will show, the terbium intensity changes with the nanoparticle growth time (vide infra).

3.1.2 Transmission Electron Microscope Imaging

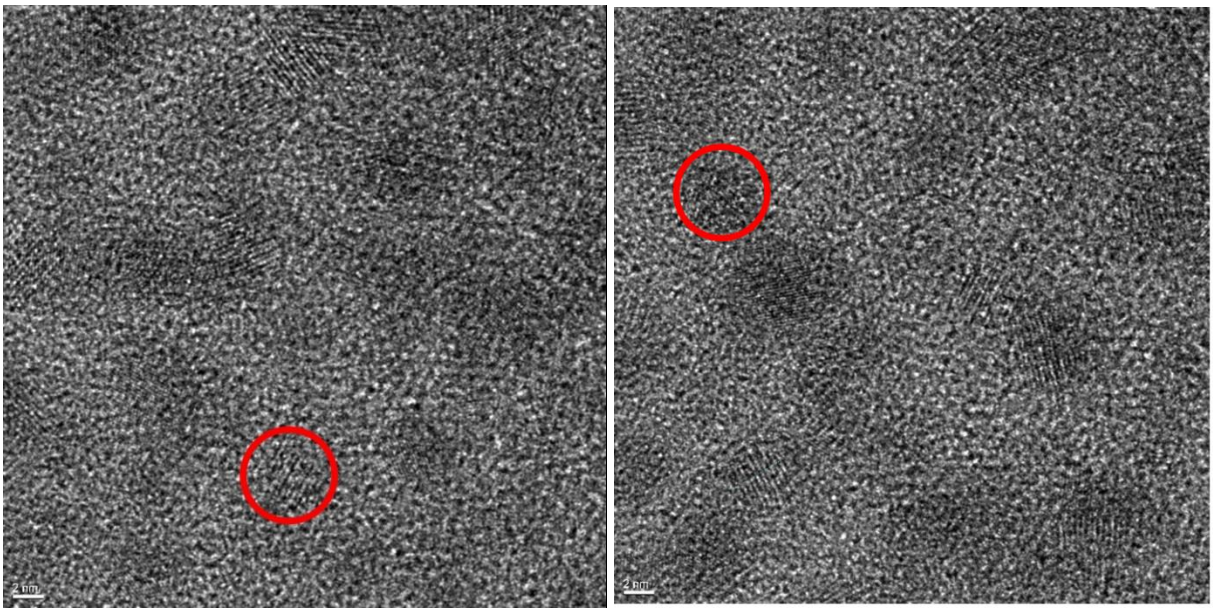

Figure 11: TEM images of CdSe:Tb particles. The scale bars are 2 nm. Crystal structure is easily observed in these images, verifying that nanocrystals are present.

The TEM images in figure 11 show CdSe:Tb nanocrystals have formed. The bottom left corner of each image shows a scale bar that is 2 nm. Thus the particles in this image are ~ 5 nm in diameter and show crystalline characteristics. The red circles in the images show an example of a single nanocrystal. Looking closely, the lattice is observed. These appear as a set of lines that run parallel, intersected by a second set of lines running perpendicular to give a grid pattern. These grids show the crystalline nature of the particles, and that they are not amorphous. Not only is it important to determine the presence of nanoparticles, but it is imperative to examine the elemental composition of the particles. For this purpose, EDS was utilized.

3.1.3 Energy Dispersive X-Ray Spectroscopy

EDS is one method of determining elemental composition. Each element has characteristic energy levels that can be detected using this technique. A core electron is ejected

from the atom via a high energy electron beam. An outer shell electron then fills in this hole and in the process releases an X-Ray with an energy that is representative of the atom from which it was emitted. EDS analysis was performed on these particles and the data are shown below in figure 12. Peaks that appeared in the spectrum belong to Cd, Se, and Tb, as can be expected for the particles. Multiple peaks are present due to a distribution of energies that are observed when an electron relaxes from one of several high energy states to a lower energy state. In quantifying the percentages of each element, however, only one main peak is used. The software analyzes the peak heights and determines an overall percentage for the elements quantified. In these data, Cd, Se, and Tb were the only elements that were quantified because we needed to find the ratios in which these elements were present in the nanoparticles. Also, there are peaks present for Cu, which is present because the sample grid is a copper grid. The grid itself is coated with a thin carbon film, which allows for the nanoparticle sample to bind to the surface and remain present on the grid while the solvent evaporates off. The background of the TEM images, meaning where nanoparticles are not located, shows the carbon film. From EDS measurements, atomic percentages were calculated.

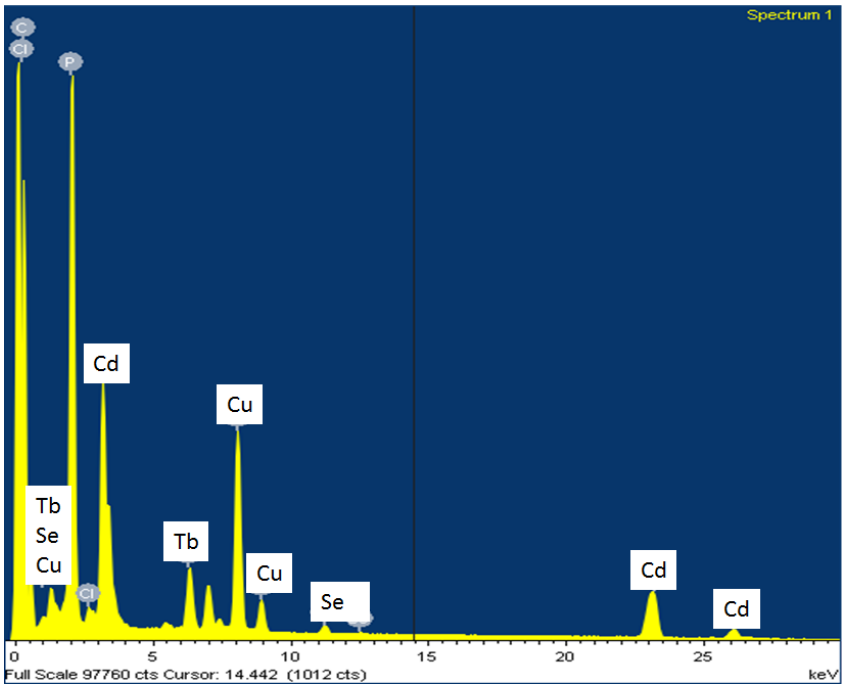

Figure 12: EDS data shows presence of Cd, Se, and Tb. Also present is Cu, which is the sample grid.

Table 1: This table shows the number of atoms calculated for each sample based on the particle diameter. Also presented is the percentage of terbium present in the sample, as determined by EDS measurements. Finally, the total number of terbium ions in each nanocrystal is calculated based on these two pieces of data

Sample	No. atoms	No. Cations	% Tb	No. Tb
5	145	72.3	24.45, 10.21	17.7, 7.38
6	156	78	36.24	28.2
7	158	79.1	7.95	6.29
8	175	87.6	26.83, 3.93	23.5, 3.44
9	191	95.3	3.46	3.3
10	218	109	27.12	29.6
11	245	123	18.76	23
12	306	153	11.25	17.2

In order to determine the number of atoms present in the nanoparticle, and therefore the number of terbium ions present, the size of the particles needed to be determined. Using an approximation determined by Peng, et al. the diameter of the particles was calculated based on their first exciton absorption peak, and these values are reported in the table of figure 10. A

study by Sarma, et al.[xxiii] gives an approximation, shown in equation 6, for the number of atoms by using a lattice spacing for CdSe of 6.05 Å and assumed a spherical shape. The number of atoms is calculated from the diameter of the spherical particle, with a constant spacing between each atom.

$$d = a\left[\frac{3N}{4\pi}\right]^{1/3} \tag{6}$$

The number of atoms, N, is calculated from the diameter, d, of the spherical particle, with a constant spacing between each atom, a.

To determine the number of terbium ions, some additional assumptions were made. First, the number of cations and anions was assumed to be in a 1:1 ratio for calculations. The number of atoms in each particle ranged from 145 for the smallest particles to 306 for the largest particles based on equation 6, therefore the number of cations ranged from ~72 to 153. EDS reported the atomic percentage of each element present, including Cd, Se, and Tb. Using the ratio of Cd:Tb found by the instrument, and the total number of cations in the particle, the number of terbium atoms was calculated. Depending on the position of the grid being analyzed, however, different values were found. For example, in samples five and eight, EDS measurements were taken at two regions of the copper grid. Each spot produced drastically different data. In sample eight, it was found that while one spot had only ~3 terbium ions per particle, another spot from the same sample had ~24 terbium ions. This variability caused us to conclude that the EDS data measurements were not reliable.

3.1.4 Time-Gated Fluorimeter

Time-gated fluorescence measurements were used to isolate the terbium emission signal and to quantify how its intensity depends upon the bandgap of the host material. These data were collected with a delay time of 0.100 ms. This delay time would only collect fluorescence that was emitted 0.100 ms or more after the flash of the excitation source, eliminating the nanosecond timescale background fluorescence, and only a signal from the long-lived luminescent species remained; more particularly, the signal from terbium. The intensity of the terbium ion was adjusted for the optical density of the nanoparticle solution and showed an overall decrease in intensity as the bandgap of the nanoparticle decreased. As can be seen in figure 13, the largest bandgap of 2.53 eV, gave the most intense terbium emission signal. As the particle growth time increases their respective bandgaps decrease, and emission signal decreases. A clear correlation between the emission intensity and the bandgap, or size, of the nanoparticle is evident. A second example of this is shown in figure 23 in the appendix.

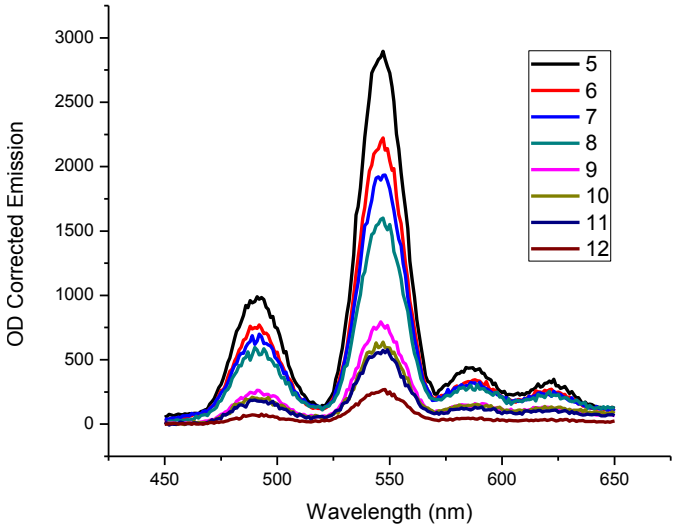

Figure 13: Time-gated terbium emission from CdSe;Tb nanocrystals. Samples 5-12 represent the varying size and bandgaps of the host particles used. For sample 5, the bandgap is 2.72 eV while for sample 12 the bandgap is only 2.53 eV.

Figure 14 shows an excellent correlation between the emission intensity and the bandgap of the nanoparticle, without considering the concentration of terbium ions giving rise to the emission intensity. The sensitization of the Tb^{3+} emission by the nanoparticle was confirmed by measuring the excitation spectra of the different nanoparticles (see Appendix A.2) Based on the model proposed by Mukherjee, it is expected that the larger bandgap hosts should sensitize the lanthanide ions more efficiently than small bandgap hosts. As the model predicts, at large bandgaps, the conduction band edge increases above the excited state of the terbium and allows for efficient energy transfer and luminescence. With smaller bandgap hosts, the conduction band edge is lower than the excited state of the terbium, and non-radiative quenching is important. The terbium is also able to function as a hole trap because the ground level lies above the valence band edge of the CdSe host.

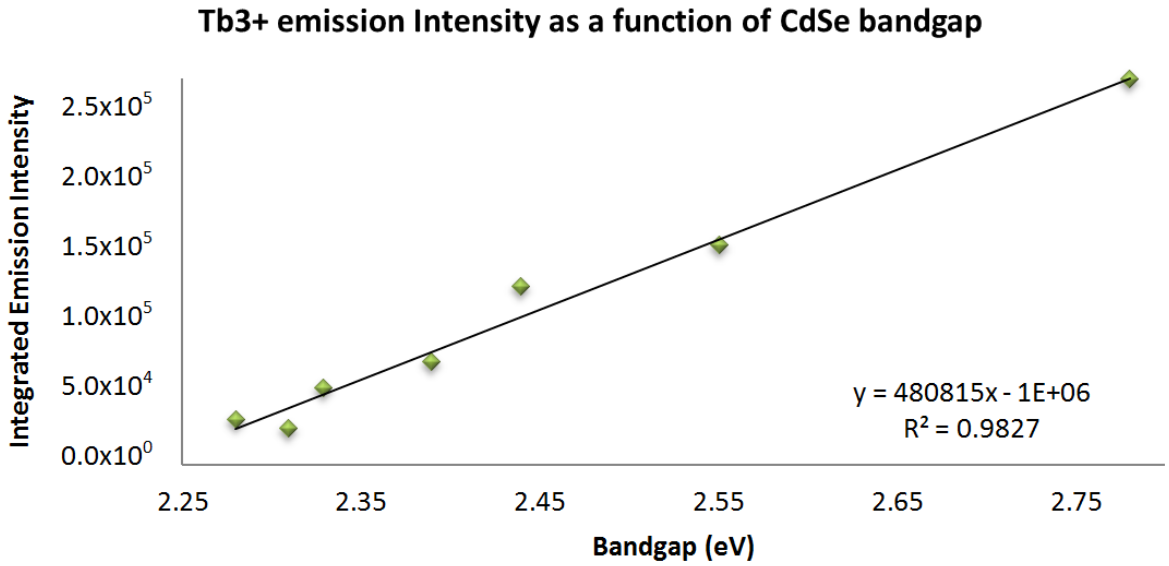

Figure 14: This plot shows the correlation (R^2 = 0.9827) between the bandgap of the nanoparticle and the overall terbium emission observed. This correlation does not account for varying concentrations of terbium ions in the nanoparticles.

To quantify the changes in Tb^{3+} emission intensity with the nanoparticle bandgap, we attempted to quantify the amount of Tb^{3+} in the nanoparticle as a function of size. Although the EDS measurements were not very precise for quantifying the the Tb^{3+} concentration in the nanoparticles, see section 3.1.3. These Tb^{3+} concentrations were used to scale the strength of the luminescence signal and find the emission strengths per Tb^{3+} ion. Table 2 shows a compilation of these data. Figure 15 shows a plot of these data as a function of the bandgap; all EDS measurements were considered. Although the intensity of Tb^{3+} is low for low bandgap nanoparticles and there is some increase of intensity with increasing bandgap, the data is scattered and a number of data points do not follow this trend. Note that points at 2.62 eV and 2.72 eV each have two values, which is due to the EDS measurements varying at two locations on the sample grid. The open squares on the graph mark the average of the two values. While

the use of the averages improves the correlation, the scatter in the raw data was deemed unacceptable.

Table 2: These data show the total overall integrated emission from time gated luminescence measurements, and the emission intensity per Tb^{3+} ion. The number of terbium ions is carried from table 1. Multiple values correspond to two locations on the copper grid where data was collected.

Sample	No. Tb	Corrected Integrated Emission	Emission/Tb ion
5	17.7, 7.38	1.22×10^5	6.91×10^3, 1.65×10^4
6	28.2	9.40×10^4	3.33×10^3
7	6.29	8.59×10^4	1.37×10^4
8	23.5, 3.44	7.37×10^4	3.14×10^3, 2.14×10^4
9	3.3	3.59×10^4	1.09×10^4
10	29.6	3.14×10^4	1.06×10^3
11	23	2.79×10^4	1.21×10^3
12	17.2	1.13×10^4	6.60×10^2

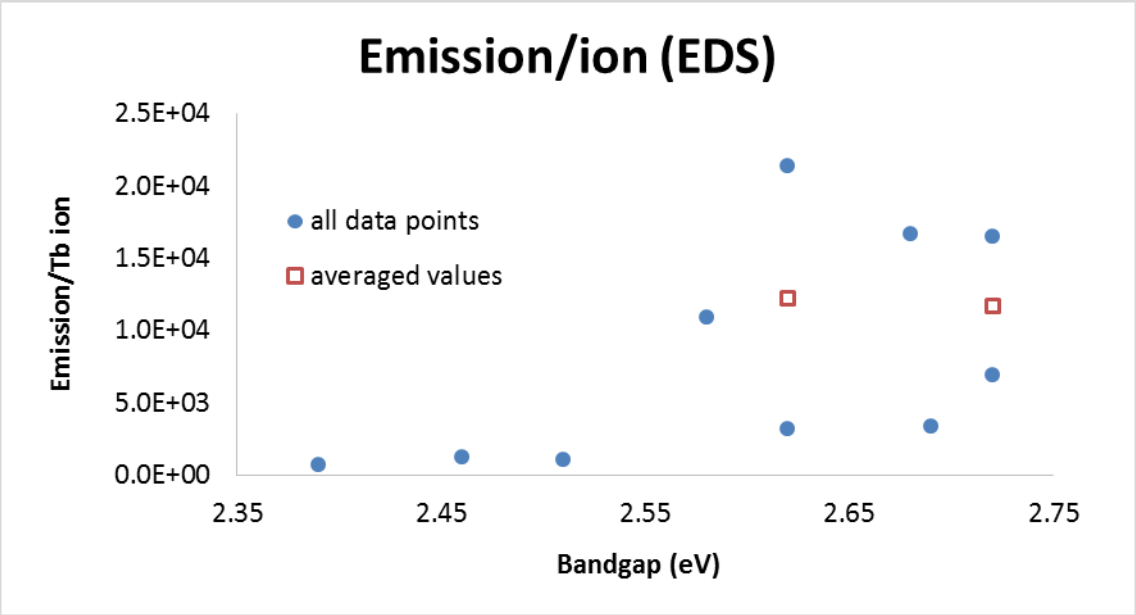

Figure 15: The correlation between integrated emission per terbium ion and host bandgap as determined by EDS represented by circles. The open squares represent average values for those points where multiple measurements were made.

Because EDS was not able to give consistent results, or did not account for some sample heterogeneity in the sample, it was not a useful technique for evaluating whether the changing emission intensity arises from a change in Tb^{3+} concentration or a change in the bandgap alone. Because of these results, we found that EDS was not the most reliable source and it would be best to test an entire aliquot that had been removed from the reaction vessel to obtain an average Tb^{3+} concentration. For these reasons, we next pursued ICP-AES. These findings were confirmed by repeating the entire study and these data are provided in the Appendix.

3.1.5 Inductively Coupled Plasma Atomic Emission Spectroscopy

In order to improve the determination of the average terbium ion concentration in the nanoparticles, an analysis that uses a larger quantity of nanoparticles was used. An entire aliquot was digested completely and run as one sample, thus allowing for a measurement that would be averaged over the entire sample. The ICP technique determines the elemental composition of each sample based on the detection of atomic emission lines. Because ICP has very low limits of detection, generally on the order of ppm to ppb, it was a sufficiently sensitive method to determine the amount of terbium ions present in the sample solutions. ICP is also able to distinguish among many elements because there is little to no overlap in atomic emission lines, allowing for optimal resolution between peaks.

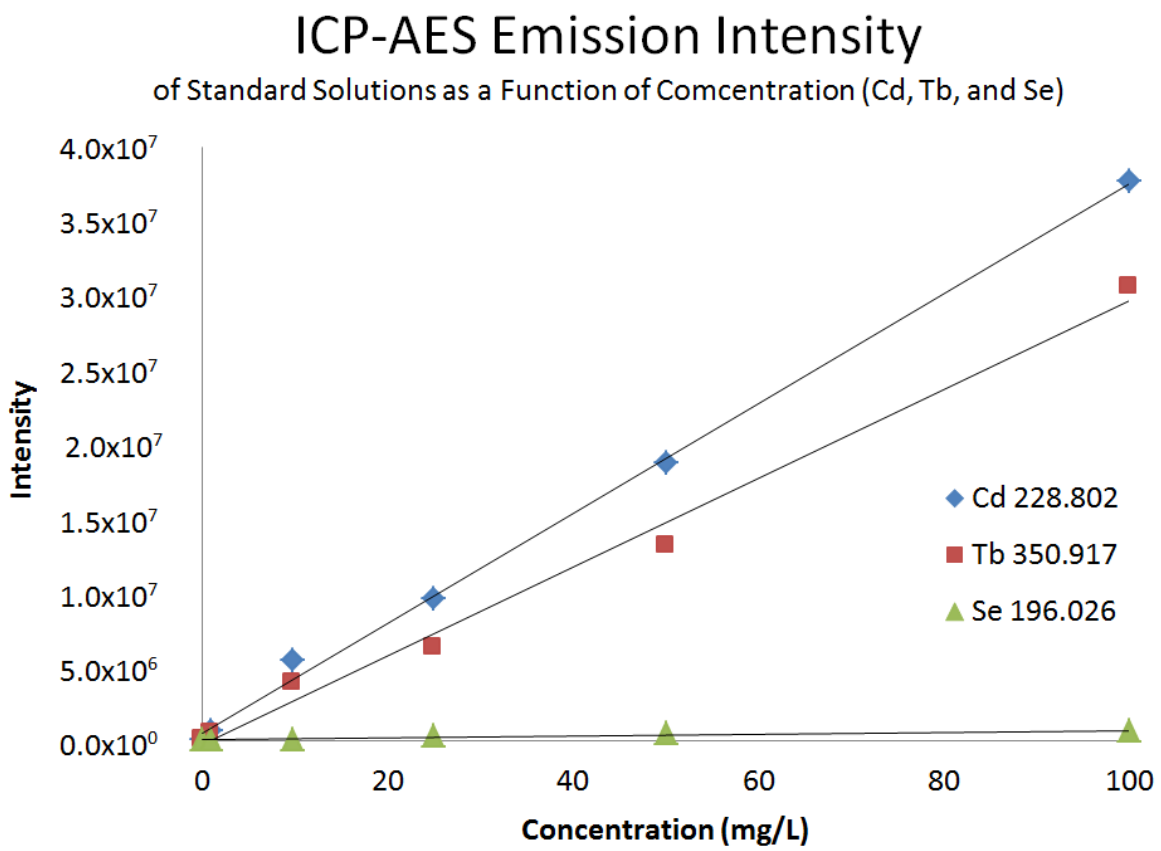

Figure 16: Calibration curves for ICP-AES data showing the correlation between intensity and concentration with R^2 values all above 0.99.

Concentrated stock solutions of Cd, Se, and Tb salts were diluted with deionized water to make calibration standards ranging from 0-100 ppm and they were run through a PerkinElmer ICP-AES. The standards used to make these stock solutions were aqueous salts in a three to five percent nitric acid solution. The calibration curves yielded a very high correlation between concentration and atomic emission intensity. The emission lines that were used for Cd, Tb, and Se, were 228.80 nm, 350.92 nm, and 196.03 nm, respectively. Each element shows a different sensitivity. This can be seen by the different slopes for each of the elements tested having a different value and instrument response. At 100 ppm, the Cd intensity was nearly 3.77 x 10^7 counts, while the Tb was 3.06 x 10^7 counts, and Se was just 6.65 x 10^5counts. The high R^2

values show a very strong linear correlation between concentration and intensity, making it a suitable technique to test for these elements over a broad range of concentrations.

The instruments software gave intensity values for each element present. These values were corrected by a blank subtraction and normalized to an internal standard, Y. These intensities were then fit to the calibration curves of the standards which were corrected in the same manner. Using the calibration curve, the given intensity allowed for the determination of the concentration in ppm, or mg/L. The total sample volume was taken into consideration to give the total mg of each element present per sample. These mass values were converted into moles using the average atomic mass of each element; the mole values of each element were summed and normalized to 100%; and each element had a corresponding percent composition of the nanoparticles. These percentages were then used in the same way they were for EDS calculations. This mean the particle diameter was used to find the total number of atoms, and then the newly calculated percentages from ICP yielded a number of terbium ions giving rise to the fluorescent signal.

Once the concentrations for terbium were calculated, the comparison was made between emission intensity per terbium atom and the band gap of the host. Much like in the EDS experiments, the emission area was integrated and normalized to the number of terbium ions found. This value, emission per ion, was then compared to the host bandgap to see if there was a correlation. Figure 17 shows a plot of these data. It is evident from the plot that considerable scatter remains in the data set.

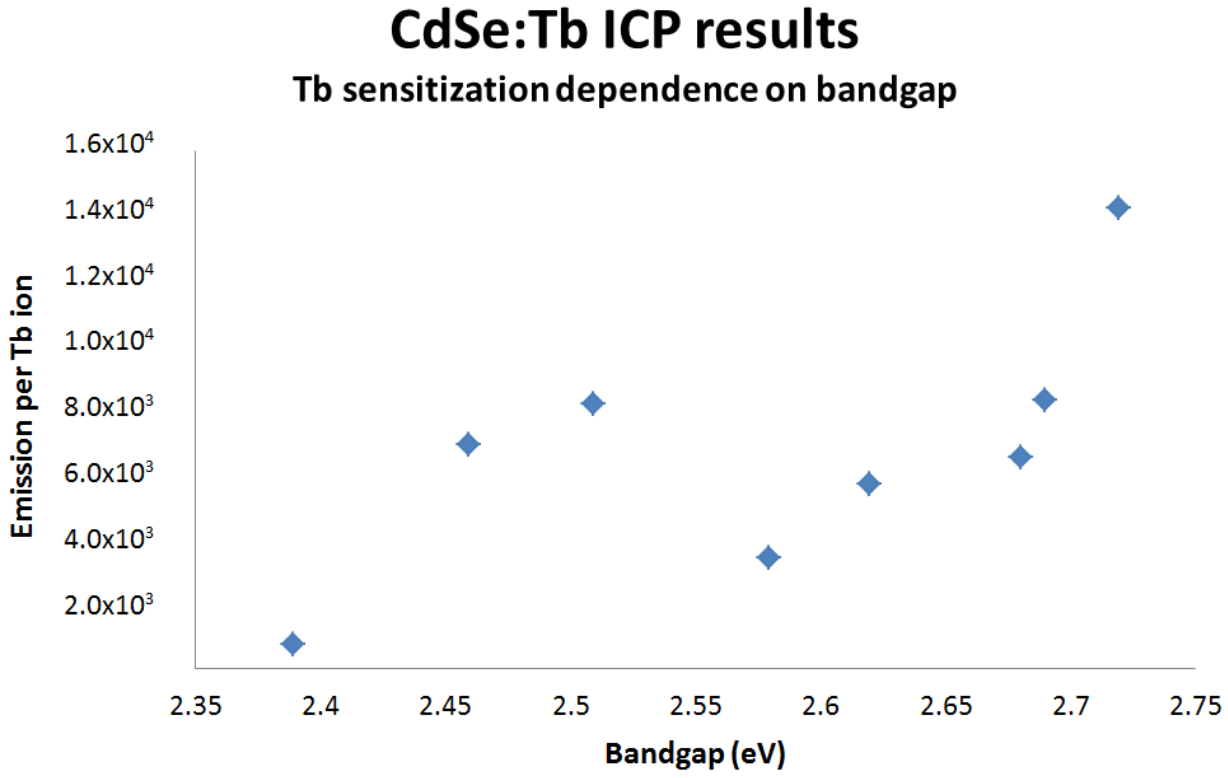

Figure 17: This plot shows the correlation between host nanoparticles bandgap and the emission per terbium ion as determined by ICP analysis.

A trend would appear if the data points at 2.46 eV and 2.51 eV were not unusually high. It is possible that these were not repeatable; however, only one run of the ICP data was able to be performed. Samples were run in triplicate on the instrument and error was negligible. Figure 16 shows the weak relationship between host bandgap and average terbium emission per ion, as determined by ICP analysis.

A comparison of EDS and ICP was made and the results are as shown below in figure 18. In both sets of data, there is significant scatter and the lack of a clear correlation between the host nanoparticles bandgap and the terbium emission. There is a general increase in terbium emission, however, the spread in the data does not allow for any conclusions to be drawn.

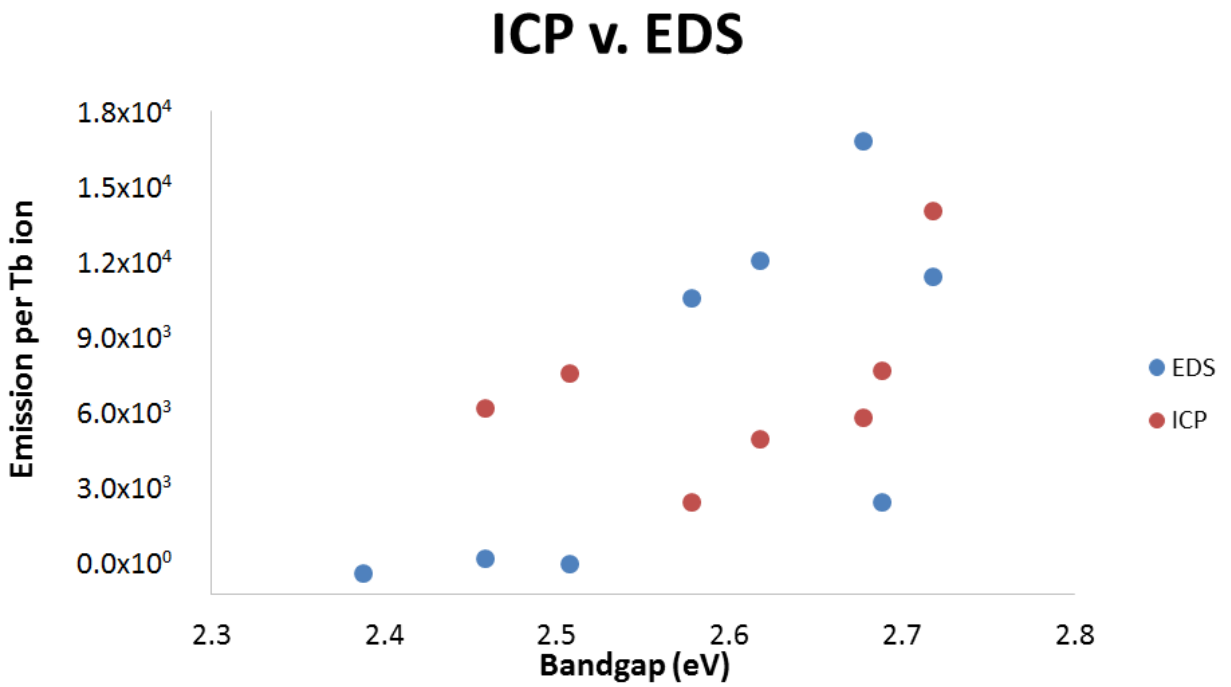

Figure 18: This shows a comparison of data obtained from EDS and ICP analysis. These data are showing the relationship between the bandgap of the host particle and the terbium emission based on the two methods tested.

The ICP data indicates an unexpectedly high concentration of cadmium. Based on data from the calibration curves, if Cd and Se were in a 1:1 ratio, the intensity of the cadmium signal should be 50 times larger than that of selenium. When the nanocrystals were being investigated, however, the signal intensity of the Cd peak to the Se peak ranged from 100:1 to 350:1, indicating a two to seven times excess of Cd. In order to understand why a large excess of Cd might be present, several possibilities were considered. We considered that the entire surface was a layer of cadmium, however this still did not explain the large excess as Cd levels were still roughly 1.5-3 times larger than this would allow. Assuming the entire surface of the crystal was Cd, this would lead to an increase in the Cd amount in the particles, while still having the same amount of Tb and Se present. These adjustments would mean the Cd signal would only be in

excess by 1.5 to 3 times. Data still showed a Cd signal of seven times that of the Se signal, which we cannot explain.

We also considered that Se may be escaping during the digestion process and proceeded to do a nitric acid digestion under reflux so that if any Se compounds were formed, the would not be able to evacuate the reaction vessel. More specifically, in the first method of digestion, nanocrystal samples were placed in vials with nitric acid. Nitric acid was added directly to these vials while open to the air, and then the vials were heated to just boiling. Aliquots of nitric acid were added until the solution appeared clear, indicating a complete digestion. ICP data from this method showed abnormally high amounts of Cd present, when compared to the selenium present. In other words, the ratio of Cd:Se was much higher than unity. In the second method of digestion, the vials were kept under reflux to eliminate the possibility that Se was forming a gas and escaping the vessel. However, when these data were compared to method one, there was not a significant reduction in the ratio of Cd:Se.

3.1.6 X-Ray Photoelectron Spectroscopy

Lastly, XPS was attempted to determine the elemental composition of the nanoparticles. XPS is a technique that can be used for surface analysis on thin layers, generally 10 nm or less. Because our particles were small in size, less than 5 nm, XPS was theoretically useful in determining the composition of a thin film of the entire particle.

Purified and powdered nanocrystal samples were placed on an epoxy resin that was on top of a tantalum foil. This foil was placed on a copper plate in the XPS. The instrument used was built in-house and used a pass energy of 50 eV. All tests were run under high vacuum and

used an Al anode at 1487 eV. Each elements binding energy regions were scanned to confirm their presence.

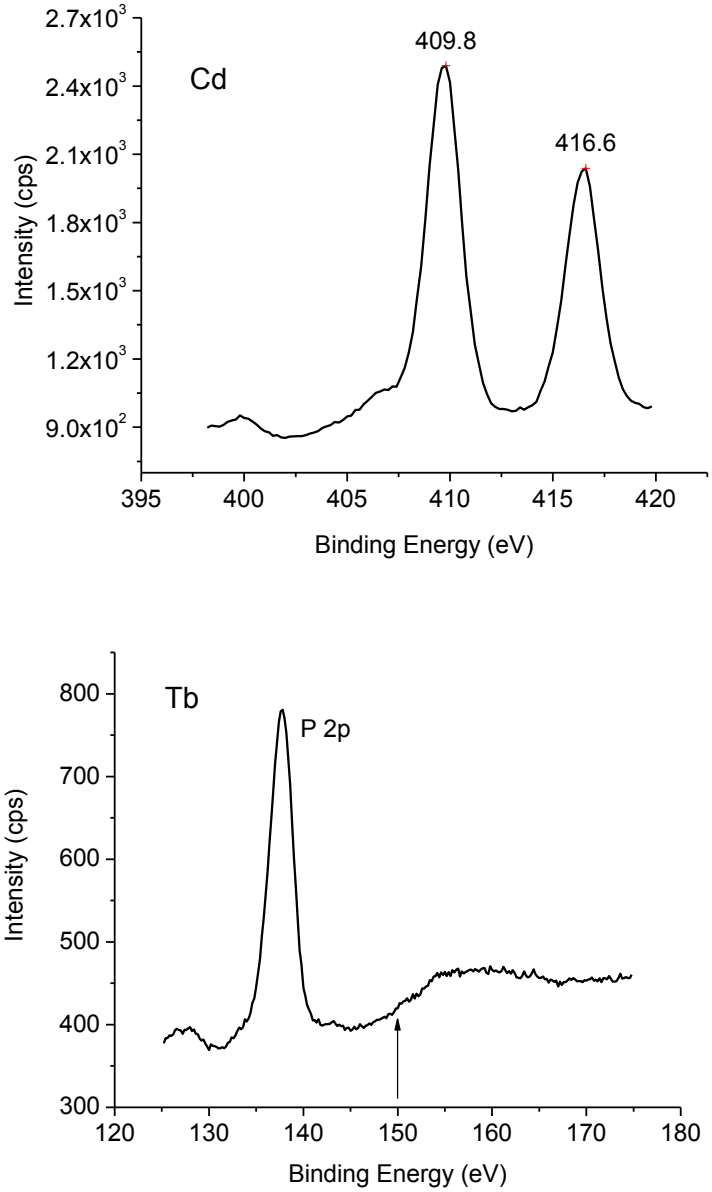

Figure 19: This data show the intensity of emitted X-rays as they relate to binding energy. XPS scans of Cd (Top) and Tb (Bottom). While Cd is easily observed, the Tb was not detectable. The arrow shows where a Tb signal should be present. Nothing is observed except a nearby phosphorus peak, which is likely due to the surface ligands.

Survey scans were taken over a wide range of binding energies, usually from 0 eV to 1000 eV. Known regions of characteristic lines were then scanned to look for the presence of each element of interest; including Cd, Se, Tb, and P. Phosphorus was used in the synthesis process and we simply tested to see if there was possibly a layer of excess ligand that could have masked the signal from Tb. The data shown in figure 18 reveals the presence of Cd, but not of Tb. The top Cd plot has peaks at 409.8 eV and 416.6 eV that represent photoelectrons originating from Cd $3d_{5/2}$ and $3d_{3/2}$, respectively. Tb should have had a peak at ~150 eV but there is no peak observable above the noise level.

Because XPS was not able to adequately detect the amounts of Tb present in the nanoparticles, it was not possible to perform measurements on a series of nanoparticle samples. Much like the results from EDS and ICP, we were unable to accurately quantify the amount of terbium present in the samples.

4.0 SUMMARY

4.1 RESULTS SUMMARY

As nanocrystals nucleate and begin to grow, we can study changes in their optical properties to learn about lanthanide sensitization efficiency. Through absorption measurements, we can see the growth of the particles by the red-shifting of the exciton peak position with growth time. These peak values also allow us to determine the optical bandgap of the host materials. As seen in figures 10 and 21 in the appendix, we can control the size of the nanoparticle hosts we are forming by controlling the growth time. Because the bandgap of the host changes with its size, this methodology provides control over the bandgap. The spectra in Figure 7 for CdSe:Tb solutions show that the nanoparticles act as an antenna to sensitize the lanthanide ions. The terbium emission intensity also shows an excellent correlation with the nanoparticle growth time.

Other host materials were attempted in this research, such as ZnS. In this case, the ZnS particles grew very rapidly and the size was not controllable. In each case, the emission and absorption spectra were very similar with no shifting exciton peak to be observed. Because of this, there was no range in bandgaps to be studied. There was also no sufficient protocol for purification which would allow imaging techniques such as TEM to be performed, or other

analytical techniques, such as ICP, which would require that the samples be free of unreacted precursors or by-products of the reaction.

Many techniques were attempted in order to quantify the number of terbium ions present in the nanocrystal samples. There was great difficulty and problems faced in each technique. EDS showed that there was an inhomogeneity in the sample grid preparation which led to unreliable results. ICP analysis showed an excess of Cd in the nanoparticles which was not explained by the testing performed here. It is possible, however, that there was excess Cd that formed a cadmium-based polymer that remained in the solution during the purification steps. Although this is hypothetical, it might be able to explain the high levels of Cd found. One brief experiment was performed by forcing the formation of the polymer. This was done by heating the cadmium precursor under the same reaction conditions as the nanoparticle growth, but without introducing the selenium and terbium precursors. If a polymer had formed under the normal reaction conditions, this process would mimic those conditions, producing the Cd polymer that was thought to be in solution causing the excess Cd. However, when we attempted to dissolve the product into solvents for NMR studies, we found that it was not soluble in any of the solvents that the nanoparticles are routinely studied in. The difficulty in making a solution of the polymer from the powder suggested that this was not the explanation for the unusually high Cd amounts, since if a polymer had formed during the synthesis and was present in ICP measurements, the solvents would have been able to effectively solubilize the polymer. The difficulties in XPS are also unclear. The samples were sent out to another facility as well, but they were not able to detect terbium either. XPS should be able to detect terbium

to less than one percent, but the experiments performed herein did not successfully quantify the terbium levels.

Although a clear correlation between the Tb^{3+} luminescence intensity and the nanocrystals growth time exists, one would expect a more dramatic decrease in Tb^{3+} luminescence intensity with growth time than what is seen. During the synthesis, 15% terbium is added to the reaction mixture. If this amount is incorporated into the final product, the emission dependence on the bandgap would be amplified. This is due to the difficulty in incorporating terbium ions into smaller particles. If there were a constant percentage in each nanoparticle, and the bandgap effect was still prominent, the smaller particles would be sensitized most efficiently, and have only several terbium ions. The larger particles would not only sensitize the terbium less efficiently, but they would also contain a larger number of terbium ions, making the emission per ion value significantly less. For example, refer to Table 3 to see the number of terbium ions that would be projected in the final product. The emission values are those reported previously in table 2. In this calculation, it is assumed a constant 15% of terbium ions in every nanoparticle. Using these data, there is an exponential correlation as shown in Figure 20. This means that under ideal circumstances, these are the data that would be observed, and there would absolutely be a trend between the host bandgap and the emission from the terbium ions.

Table 3: This table shows the calculations for an ideal system where 15% Tb is incorporated evenly into each aliquot. The samples, bandgaps, total atoms, and total emission are the same as used in prior calculations for EDS measurements.

Sample	Bandgap (eV)	Diameter (nm)	Total atoms	Total cations	No. Tb (15%)	Total Tb^{3+} Emission	Emission/Tb ion
5	2.72	1.97	145	72.3	10.845	1.22×10^5	1.13×10^4
6	2.69	2.02	156	78	11.7	9.40×10^4	8.03×10^3
7	2.68	2.03	158	79.1	11.865	8.59×10^4	7.24×10^3
8	2.62	2.10	175	87.6	13.14	7.37×10^4	5.61×10^3
9	2.58	2.16	191	95.3	14.295	3.59×10^4	2.51×10^3
10	2.51	2.26	218	109	16.35	3.14×10^4	1.92×10^3
11	2.46	2.35	245	123	18.45	2.79×10^4	1.51×10^3
12	2.39	2.53	306	153	22.95	1.13×10^4	4.94×10^2

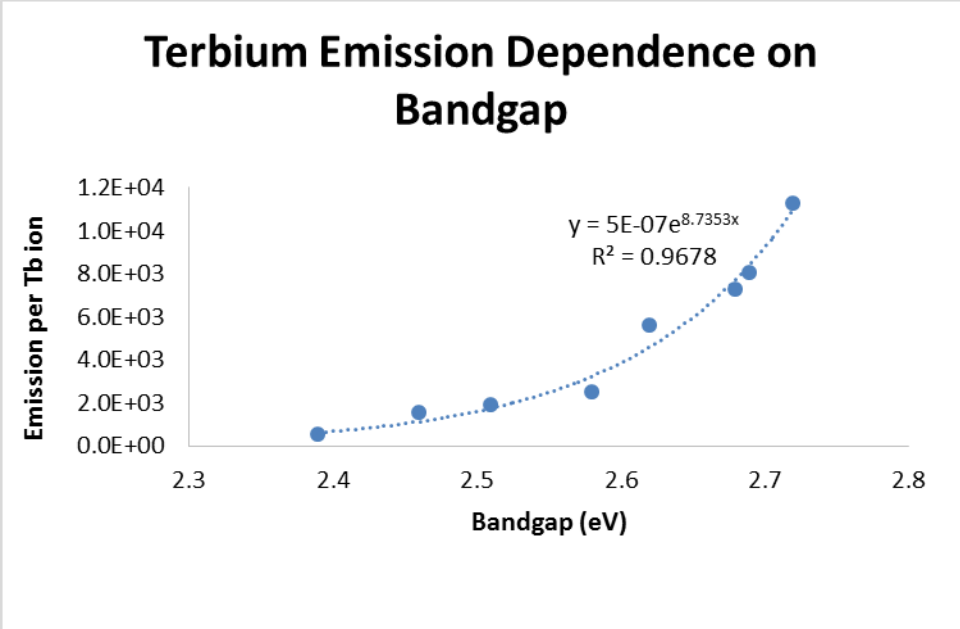

Figure 20: This graph shows the exponential correlation between the emission per Tb ion and the host bandgap when a consistent doping percentage of 15% is used.

Another effect worth mentioning is that in smaller nanoparticles, with larger bandgaps, it is unlikely that Tb^{3+} can incorporate as a dopant in the core of the particle. The lattice strain would increase drastically. Thus, the terbium dopant would reside closer to the surface of the nanoparticle host. These terbium emitters at the surface are less protected from non-radiative decay pathways, and are susceptible to being quenched by the solvent or surface ligands. If these dopants were protected from non-radiative decay, their emission signal could potentially be even more amplified than is shown in Figure 20. For example, if a small particle with very intense emission were able to incorporate Tb^{3+} that were not quenched by solvent and ligands, their emission would be more significant. A possible way to investigate this effect would be to protect the core nanoparticle by adding an inorganic shell type nanoparticle, such as ZnS. This would protect the terbium from solvent quenchers, and possibly allow a much stronger signal!

Further testing could be done to try to accurately determine the terbium levels present in the nanoparticles. Only one run was performed for ICP, and because of its sensitivity and ease of use and preparation, it would be interesting to see if this method was optimized whether results could be obtained.

Although there were limitations to the quantification of terbium ions which would allow for an accurate emission intensity per Tb^{3+}, this study demonstrates that emission intensity is related to the growth time of the host nanoparticle. If the dopant concentration could be accurately determined, then one could determine whether the luminescence intensity per Tb^{3+} ion increased and hence gain insight into the mechanism of the sensitization process. Despite the scatter in the EDS and ICP determinations of Tb^{3+} concentrations, the luminescence intensity per Tb^{3+} ion showed a general increase with nanoparticle bandgap. While only qualitative, the

general trend suggests that the energy transfer model is a good predictor of sensitization; however, further testing needs to be investigated before concrete conclusions can be made.

APPENDIX

A.1 EXAMPLE

The growth of the nanoparticles was determined from the absorption measurements. As the reaction time increased, the absorbance peak red-shifted and the nanoparticles grew in size. Figure 21 below shows an example of the absorbance peaks shifting from 444 nm to 542 nm. These peak positions have corresponding bandgaps and particle diameters, as shown in table 4. The smallest particle with an absorption peak at 444 nm corresponds to a bandgap of 2.78 eV and a particle that is 1.91 nm in diameter.

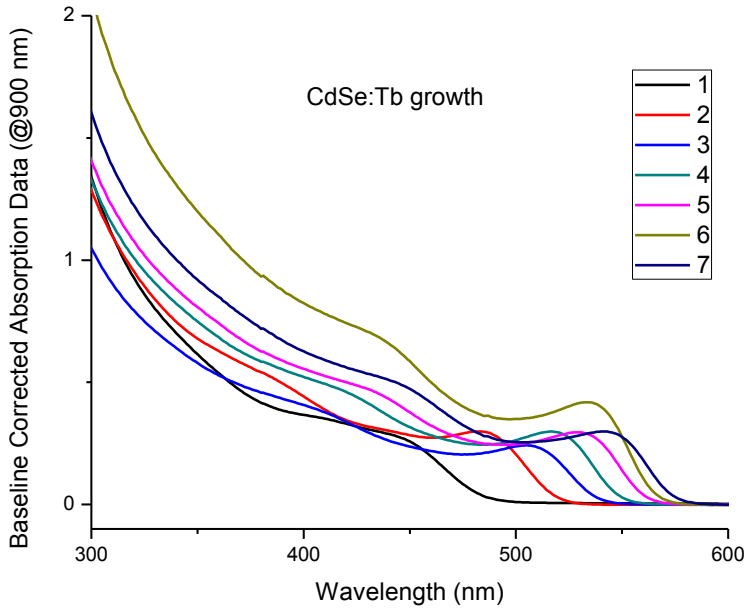

Figure 21: This plot shows the absorbance spectra of a second batch of CdSe:Tb nanoparticles. The peaks shift from 444 nm to 542 nm.

Table 4: This table shows the nanoparticle size dependence on the growth time and absorption peak position

Sample	λ_{max} (nm)	Bandgap (eV)	Diameter (nm)*[xxiv]
1	444	2.78	1.91
2	484	2.55	2.21
3	505	2.44	2.39
4	517	2.39	2.53
5	530	2.33	2.70
6	534	2.31	2.76
7	542	2.28	2.89

A.2 ANTENNA EFFECT

In order to show that the terbium was not directly excited, but rather was sensitized by the nanoparticle antenna, their excitation profiles were investigated as well. Figure 7 demonstrates the excitation spectra for terbium when it is directly excited; there are many sharp atomic transitions present in the excitation profile. When terbium is sensitized by the antenna like that shown in figure 22 its profile changes drastically to show one broad band. There is a lack of direct excitation bands like shown in figure 7 for the free terbium in solution. This broad band is similar in shape and position to the CdSe host excitation. It is evident that the CdSe nanoparticle is acting as the antenna due to these trends in the excitation spectra.

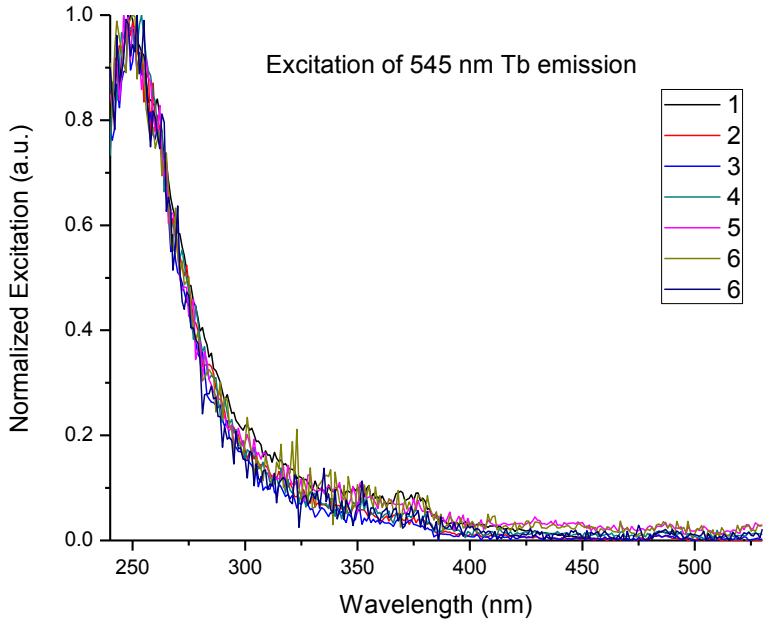

Figure 22: This plot shows the excitation spectra of CdSe:Tb nanoparticles created throughout these experiments showing the broad excitation band centered at ~250 nm. λ_{em} = 545 nm**.**

A.3 LUMINESCENT EMISSION

By varying the exciton peak position, the emission intensity is affected, as can be seen in Figure 23 and table 5 below. It is clear that aliquot 1, which is the smallest particle and has the largest bandgap, has the most intense fluorescence peak, and the intensity decreases as the nanoparticle diameter increases and the corresponding bandgap decreases from aliquot 1 through aliquot 7. The terbium emission is decreasing as the absorption peak red shifts. These data show that the bandgap of the nanoparticle is an important factor in the fluorescence intensity of the terbium ions, and that the larger bandgaps more effectively sensitize the terbium fluorescence. As the bandgap closes from 2.78 eV to 2.28 eV, the emission intensity decreases by nine times.

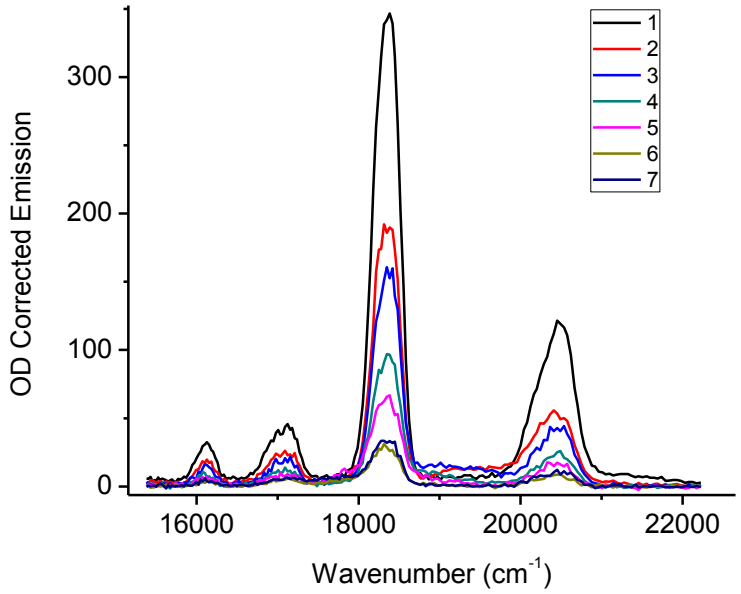

Figure 23: Time-gated fluorescence spectra of the CdSe:Tb displaying a decrease in luminescence with growth time, and thereby bandgap.

Table 5: This table demonstrates a correlation between the luminescent emission and the nanoparticle band gap.

Sample	Bandgap (eV)	Integrated Emission (a.u.)
1	2.78	263180.7
2	2.55	149823.0
3	2.44	121528.0
4	2.39	70127.6
5	2.33	52303.5
6	2.31	23792.8
7	2.28	29715.4

A.4 ALTERNATE SYNTHESIS

The nanoparticle synthesis was predominately carried out using a hexadecylamine ligand (HDA), another surface ligand was used as well. Tetradecylphosponic acid (TDPA) was used as well, and figure 24 below compares the results from two separate syntheses. It is clear that the same trend appears in both reactions, regardless of which surface ligand is used. The both show that the emission intensity is higher for large bandgap nanoparticles. These data demonstrate that the ligand chosen for the synthesis can most likely be tailored for the desired solubility or availability of ligands.

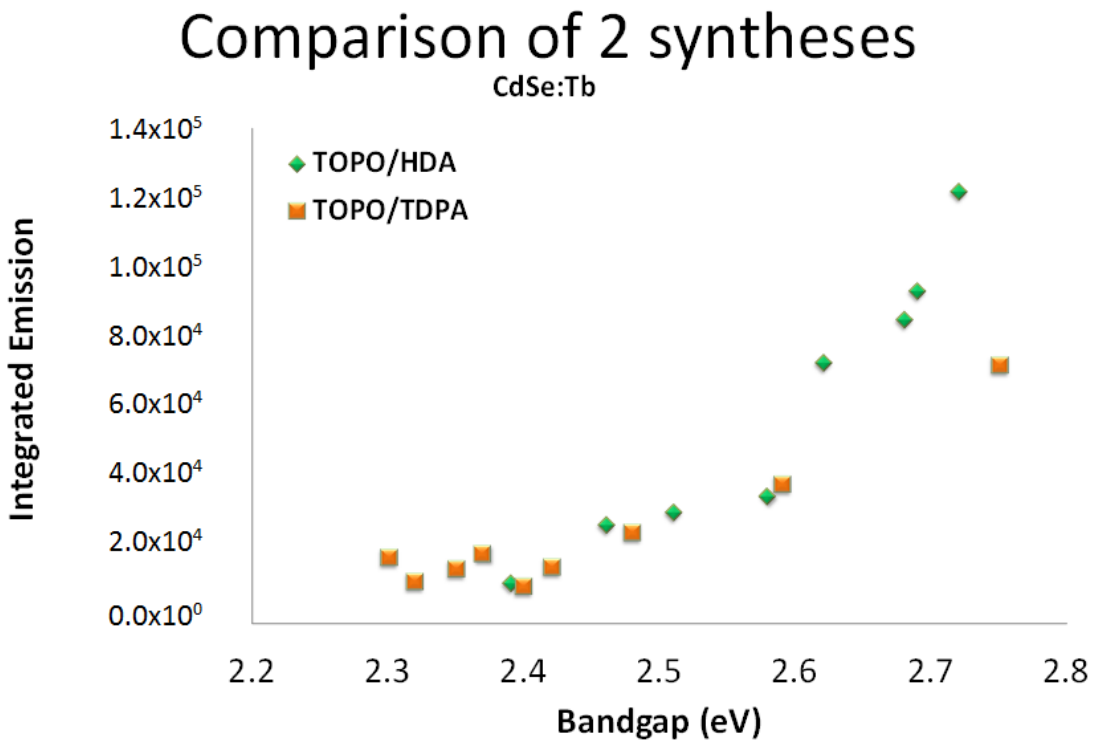

Figure 24: These data show the reproducibility between two syntheses of CdSe:Tb nanoparticles. Both syntheses used trioctylphosphine oxide (TOPO) as a solvent and ligand. One synthesis used a hexadecylamine (HDA) ligand, while the other used a tetradecylphosphonic acid (TPDA) ligand.

BIBLIOGRAPHY

[i] Mukherjee, et al. *J. Phys. Chem. A* **2011**, 115, 4031–4041

[ii] Alivisatos, A. P.; Gu, W.; Larabell, C., *Annu. Rev. Biomed. Eng.,* **2005,** *7,* 55-76.

[iii] ISS Data Tables Lifetime Data of Selected FLuorophores. "Welcome to *ISS.* ISS, Inc. Web. 29 Sept. 2011.
<http://www.iss.com/resources/reference/data_tables/LifetimeDataFluorophores.html>

[iv] Weissleder, R.; Nature Biotechnology **2001,** *19,* 316-317.

[v] Joon Won Park, et al.; Current Opinion in Biotechnology, **2006,** *10,* 423-429.

[vi] Engel, Thomas, Warren J. Hehre, and Thomas Engel. *Quantum Chemistry & Spectroscopy*. New York: Prentice Hall, 2010. 288. Print.

[vii] Zhang, J. Z., *J. Phys. Chem. B.,* **2000,** *104,* 7239-7253.

[viii] Sooklal, K.; Cullum, B. S.; Angel, S. M.; Murphy, C. J. *J. Phys.Chem.* **1996**, *100*, 4551–4555.

[ix] Kuhn, Hans, Horst-Dieter Försterling, and David H. Waldeck. *Principles of Physical Chemistry*. Hoboken, NJ: John Wiley, 2009. 373. Print.

[x] Nanocrystal Quantum Dots. Ed. Victor I. Klimov. 2nd ed. Boca Raton: CRC, 2010. 2-3. Print.

[xi] Brus, L. E.; *J. Chem. Phys.,* **1984,** *80,* 4403-4409.

[xii] Yu, W. W.; Qu, L.; Guo, W.; Peng, W., *Chem Mater,* **2003,** *15,* 2854-2860.

[xiii] Yu, W. W.; Qu, L.; Guo, W.; Peng, W. *Chem Mater,* **2003,** *15,* 2854-2860.

[xiv] Bünzli, J.C.; Eliseeva, S., *Elements,* Publisher: Springer Berlin Heidelberg, **2009,** *7,* 1-45

[xv] Carnall, W. T., Fields, P.R., *Lanthanide/Actinide Chemistry;* American Chemical Society: Washington D. C., 1967; Vol 71.

[xvi] Beeby, A.; Clarkson, I. M.; Dickins, R. S.; Faulkner, S.; Parker, D.; Royle, L.; de Sousa, A. S.; Williams, J. A. G.; Woods, M., *J. Chem. Soc., Perkin Trans. 2,* **1999,** 493-503.

[xvii] Kröger, F. A.; Meyer, H. J. G., *Physica XX,* **1954,** 1149-1156.

[xviii] Singha, A., et al.; *J Phys.: Condens. Matter*, **2005,** *17,* 5697-5708.

[xix] Reusch, William. "Infrared Spectroscopy." *Michigan State University :: Department of Chemistry*. Web. 29 Sept. 2011.
<http://www2.chemistry.msu.edu/faculty/reusch/VirtTxtJml/Spectrpy/InfraRed/infrared.htm>.

[xx] Mukherjee, P.; Shade, C. M.; Yingling, A. M.; Lamont, D. N.; Waldeck, D. H.; Petoud, S. *JPCA*, **2011,** *115,* 4031-4041.

[xxi] Dorenbos, P., *J. Lumin.,* **2005,** *111,* 89-104.

[xxii] Dornebos, P., *J. Alloys and Compounds,* **2009,** *488,* 568-573.

[xxiii] Sarma, D. D., *Phys. Rev. B*, **2004,** *69*, 125304.

[xxiv] Peng, X. *Chem. Mater*. **2003**, 15, 2854-2860.